ACS Catalysis

Research Article

pubs.acs.org/acscatalysis

Synthesis of Nanosize Tungsten Oxide and Its Evaluation as an Electrocatalyst Support for Oxygen Reduction in Acid Media

Ying Liu, Sujan Shrestha, and William E. Mustain*

Department of Chemical, Materials, and Biomolecular Engineering, University of Connecticut, Storrs, Connecticut 06269, United States

Supporting Information

ABSTRACT: WO_3 was investigated as a possible support material for monolayer Pt ORR electrocatalysts in acid electrolyte. It was found that as-prepared Pt/WO_3 showed enhanced activity for the ORR and superior electron transfer ability compared to conventional Pt/C and bulk polycrystalline Pt. However, similar to other tungsten derived supports, most notably WC, the Pt/WO_3 electrocatalyst showed significant performance degradation that was tied directly to the formation of water-soluble hydrogen tungsten bronze (H_xWO_3) on the support surface that was identified by X-ray photoelectron spectroscopy (XPS) and transmission electron microscopy (TEM). This information, combined with previous work by our group on WC supports, are also combined to propose a series degradation pathway for WC and WO_3 supports in acid media, which is relevant for proton exchange membrane (PEM) fuel cells.

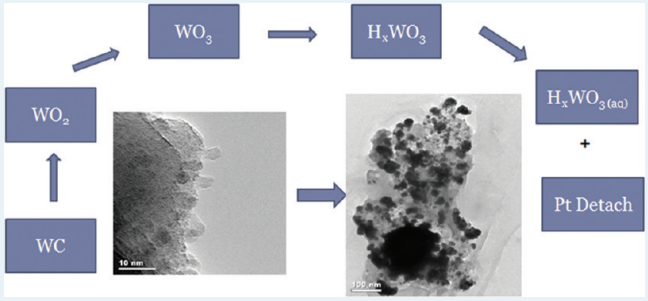

KEYWORDS: *tungsten oxide, electrocatalyst support, platinum, oxygen, reduction, catalyst*

1. INTRODUCTION

The proton exchange membrane fuel cell (PEMFC) is an electrochemical device that converts chemical energy stored by molecular hydrogen and oxygen to electrical energy through complementary redox processes. In the near future, the PEMFC is expected to play an important role in providing clean, sustainable energy for a myriad of applications because of its higher theoretical efficiency, which is not limited by traditional heat cycles. The most critical challenge in the development of PEMFCs is the discovery of low cost, high activity, stable electrocatalysts for the oxygen reduction reaction (ORR).[1−3] However, the extremely weak interaction (van der Waals forces) between the platinum catalyst and the most common support−carbon that, because of carbon's completely saturated valence shell and nearly zero unpaired surface electrons, directly leads to rapid Pt agglomeration through Pt dissolution, surface migration, and detachment during operation.[3,4] In addition, carbon itself is thermodynamically unstable at potentials >0.21 V, and this corrosion affects Pt detachment more seriously, decreasing PEMFC performance dramatically with time.[5] Most recently, significant activity and stability improvement has been demonstrated for Pt clusters on several metals, which was achieved by strong metal−support interaction.[3] It has already been shown that metal−metal bonding between Pt and the support could shift the local d-band center of Pt relative to its Fermi level,[6−8] thus changing the binding energy of atomic oxygen on the catalyst surface. This suggests that the intrinsic ORR activity of supported Pt nanoparticles can be tailored using the catalyst support and that the catalyst stability can be enhanced.[9]

Tungsten carbide and tungsten oxide have received significant attention recently since W has a large number of stable oxidation states, which enable a variety of properties for many chemical and electrochemical applications. Among all these states, hexavalent tungsten oxide, WO_3, is the most stable.[10] Although its large bandgap leads to low electronic conductivity, researchers have found that oxygen vacancies generated during the synthesis process can provide an efficient electron pathway and the conductivity of the nonstoichiometric oxides are significantly improved over WO_3.[11] Thus, tungsten oxides are considered to be a promising candidate for the electrocatalyst support at the PEMFC cathode, and several groups have already reported enhanced methanol oxidation activity for Pt/WO_{3-x} anode electrocatalysts.[12−17]

WC has been studied as an electrocatalyst support by our group[18] and others.[19,20] In our previous paper regarding Pt/WC ORR electrocatalysts, on the first scan, a clear activity enhancement compared with Pt/C was observed, which was most likely a result of pushing the Pt surface oxidation to a higher potential. However, we also found that the surface WC was oxidized to WO_x when the potential exceeded 0.8 V vs NHE, which directly led to the detachment and agglomeration of the surface Pt nanoparticles and the enhanced activity of Pt/WC was also lost.[18] Using X-ray photoelectron spectroscopy (XPS) to probe the support surface, it was found that WC, WO_3, WO_2 and carbon all existed on the surface of

Received: December 13, 2011
Revised: January 18, 2012
Published: February 10, 2012

bulk-pure WC crystals. Because of the simultaneous deformation and oxidation of the WC, the influence of the surface composition change on the activity of the electrocatalyst could not be delineated. This suggests that an independent evaluation of WO_3 as an electrocatalyst support, coupled with our previous information on Pt/WC, would allow for a new understanding of the impact of surface bonding and oxidation on the activity and stability of Pt supported on W-derived materials.

In this study, nanosized WO_3 supports were prepared, and a monolayer equivalent of platinum nanoparticles was deposited on top of the tungsten oxide crystals by galvanic displacement. In this way, a very low Pt-loading ORR electrocatalyst could be achieved. Then, the resulting electrocatalyst was characterized by X-ray diffraction (XRD), transmission electron microscopy (TEM), X-ray photon electron spectroscopy (XPS), and Brunauer–Emmet–Teller (BET) N_2 gas adsorption. Finally, the ORR activity and Pt/WO_3 stability were investigated by cyclic voltammetry (CV), linear sweep voltammetry, and chronoamperometry, and a surface dissolution mechanism is proposed.

2. EXPERIMENTAL SECTION

2.1. Synthesis of Nano-Size Tungsten Oxide Crystals. WCl_6 (99%, Acros Organics) was used as the precursor for the synthesis of nanosize WO_3 supports. First, 3.6 g of WCl_6 (dark blue crystals) was added to 50 mL of diethylene glycol (DEG, Fisher), which gave a yellow colored solution. The solution was then heated to 80 °C and gradually turned to green as the temperature increased. The reaction medium must be an organic solvent since aqueous WCl_6 can easily hydrolyze to release hydrogen chloride. Here, W(VI) was gradually reduced to W(V) by DEG to yield a dark blue, nonstoichiometric oxide precursor. Then, 10 mL of 18 MΩ Millipore deionized water was added, and the green solution immediately changed to deep blue. The resulting solution was refluxed at 190 °C for 3 h, and a deep blue suspension was obtained. The precipitate was collected by centrifuging, then was thoroughly washed with ethanol and 18 MΩ Millipore water thoroughly to remove the DEG. Finally, the precipitate was calcined in the oven at 400 °C for 3 h to form a fine, light green WO_3 powder.

2.2. Deposition of Pt on Tungsten Oxide Crystals. Pt/WO_3 electrocatalysts were prepared by depositing Pt nanoparticles on WO_3 via galvanic displacement of a Cu layer by Pt in a three-electrode electrochemical cell in N_2 atmosphere. First, the working electrode was covered with a Cu monolayer by underpotential deposition, where the electrode potential was cycled between 0.0 and 0.3 V in aqueous 0.05 M H_2SO_4/0.05 M $CuSO_4$ for 4 cycles at 50 mV/s. Then, the electrode was rinsed with copious amounts of Millipore water to remove Cu^{2+} ions from the electrode. Finally, the electrode was placed into a 0.001 M K_2PtCl_4 (Acros Organics), 0.05 M H_2SO_4 aqueous solution for 4 min. Here, one monolayer equivalent of platinum particles was formed by replacing the underpotential deposited Cu. Pt deposition on the WO_3 surface was verified by voltammetry, TEM, and XPS.

2.3. Physical Characterization of Tungsten Oxide Crystals and Pt/WO_3 Catalysts. The bulk composition of the WO_3 electrocatalyst support was confirmed by XRD with a Bruker D8 Advance diffractometer system. The morphology and nanostructure of the support was investigated by TEM with a FasTEM JEOL 2010. A Micromeritics ASAP 2020 accelerated surface area and porosimetry analyzer was used to determine the BET specific surface area of tungsten oxide. Finally, XPS performed with a Kratos AXIS-165 surface analysis system was applied to investigate the surface composition of the as-synthesized support material and the Pt/WO_3 electrocatalyst.

2.4. Electrochemical Characterization of WO_3 and Pt/WO_3. Cyclic voltammograms (CVs) of WO_3 and Pt/WO_3, recorded at room temperature using an Ecochemie Autolab PGSTAT302N potentiostat, were collected in a custom-built (Adams & Chittenden Scientific Glass) three-electrode electrochemical cell using a 5 mm glassy carbon disk electrode (GCE) as the working electrode. A Pt flag was used as the counter electrode, and a saturated calomel electrode was used as the reference electrode; however, all potentials are reported versus the normal hydrogen electrode. The GCE was polished to a mirror finish and washed ultrasonically with deionized water prior to each experiment. To disperse the synthesized WO_3 on the working electrode, an ink slurry was prepared by mixing WO_3 with Millipore water and sonicating for 20 min to make a uniform 0.3 mg/mL suspension. Then, 20 μL of the suspension was added dropwise onto the GCE with a micropipet and then dried in air for 60 min. Next, a thin layer of Nafion was deposited onto the WO_3 layer by applying 20 μL of a 0.05 wt % Nafion solution (diluted with Millipore water from 5% Nafion DE520 solution, DuPont) to prevent WO_3 detachment from the working electrode during electrochemical testing.

3. RESULTS AND DISCUSSION

3.1. Evaluation of Bulk Composition Using XRD. Powder XRD patterns of the synthesized crystals are shown in Supporting Information, Figure S1. Phase identification was done using X'pert Highscore Plus. The variation range of the diffraction angle (2θ) was from 20° to 60°, and the observed pattern corresponded well with pure crystalline tungsten oxide. Each of the observed peaks could be assigned to one of the phases of the polycrystalline WO_3. Here, the diffraction intensity of the (002), (020), and (200) crystal phases were strong at 2θ = 23.21°, 23.70°, and 24.34°, respectively.

3.2. Nanostructure of As-Synthesized WO_3 Electrocatalyst Supports and Platinized WO_3. The tungsten oxide crystals showed single spherical particles approximately 30 nm in size. From the TEM images in Figure 1a, the WO_3 was well faceted and had low internal porosity. The low internal porosity was supported by the specific surface area of the WO_3 electrocatalyst supports, determined by the BET method, where the average value of several samples was 29.9 m^2/g. This was similar to the theoretical value of 27.9 m^2/g (calculated by taking WO_3 crystal as the perfect sphere with a 30 nm diameter). Also, the BET isotherm showed the pore volume was only 0.0001 cm^2/g, which indicated that the WO_3 crystals were nonporous. Compared with previous preparation methods for WO_3 substrates, (i.e., WO_3 microspheres of 2–4 μm diameter by controlled oxidation of tungsten carbide microspheres[14]), this nanosize could help increase the surface to bulk atomic ratio of platinum, achieving a lower precious metal loading to be used on the support materials without compromising the efficiency of the whole electrocatalyst, providing a promising support for Pt cluster electrocatalysts in PEMFCs. Figure 1b shows TEM images of as-prepared Pt/WO_3 electrocatalysts. The Pt nanoparticles were dispersed uniformly on the WO_3 crystals with an average size of approximately 3 nm.

3.3. Surface Characterization of Prepared WO_3 Support. The surface composition is of primary importance in this study since electrochemical processes occur exclusively on the surface. Here, the surface composition of tungsten oxide was probed by XPS. Figure 2 shows the broad XPS spectra (a) and focused W 4f spectra (b) of the nanotungsten oxide crystals. XPS survey studies revealed the presence of tungsten, oxygen, fluorine (Nafion), and carbon (substrate). The W 4f spectrum was deconvoluted into two doublets (four peaks), and the results are shown in the Figure 2b. The binding energies of the first doublet peaks are 35.2 and 37.4 eV for W $4f_{7/2}$ and W $4f_{5/2}$, respectively, which corresponds to the WO_3 oxidation state. The second doublet peaks have binding energies at 33.9 and 35.7 eV which is consistent with pentavalent W $4f_{7/2}$ and W $4f_{5/2}$; given the synthesis processes, the most likely W^{5+} species was W_2O_5, which has been shown to be stable previously,[21] though nonstoichiometric oxides are

dx.doi.org/10.1021/cs200657w | ACS Catal. 2012, 2, 456–463

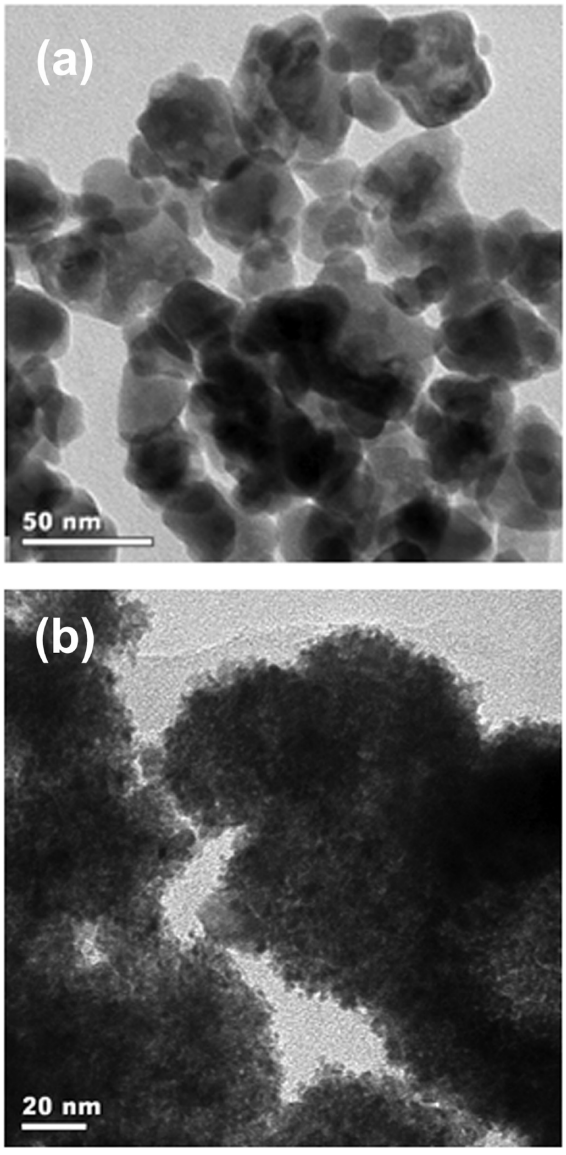

Figure 1. TEM images for (a) pure tungsten oxide crystals and (b) fresh-synthesized Pt/WO_3.

possible as well. The percentages of WO_3 and W_2O_5 were calculated as 91% and 9%, respectively. Post plantinization XPS spectra are shown in Figure 3d. An obvious Pt peak appeared in the Pt 4f region of the XPS spectra. The Pt $4f_{7/2}$ and Pt $4f_{5/2}$ peaks for the Pt/WO_3 catalyst were located at 74.04 and 70.65 eV, respectively (Figure 2d), which confirmed that Pt crystals were present on the WO_3 surface. Binding energies of the F 1S main peak, W $4f_{7/2}$ and W $4f_{5/2}$ of W_2O_5 for the WO_3 crystal are 688.15 eV, 35.25 and 37.46 eV, respectively, while those for the Pt/WO_3 catalyst are 688.13 eV, 36.11 and 38.26 eV, respectively. To inspect the W peak positions accurately, the binding energies of the W 4f are referenced to the F 1s main peak. Doing this, it was found that the position of the W $4f_{7/2}$ and W $4f_{5/2}$ peaks shifted positively by 0.88 and 0.82 V, respectively, after Pt was introduced, suggesting that a "strong metal-support interaction" may exist between Pt and WO_3. This may be due to strong orbital hybridization between Pt and WO_3 that intensifies charge transfer at vacancy sites,[22] and was not observed for Pt/WC electrocatalysts. This kind of "metal-support interaction" could inhibit the aggregation of Pt nanoparticles, keeping the high dispersion of the Pt nanoparticles and a narrow size distribution. It could also enhance the intrinsic activity of Pt for the ORR by changing the Pt−O bonding energy and improving its electron transfer efficiency.

3.4. Ferrocyanide/Ferricyanide Redox Couple. The intrinsic electron transferability of Pt/WO_3 was evaluated using the ferrocyanide/ferricyanide (FEFI) redox couple (eq 1). The FEFI couple is one of the most popular electrochemically reversible couples because of its simple reaction mechanism, a single Marcus outer shell electron transfer process with no bond breakage or reorganization steps:

$$Fe(CN)_6^{3-} + e^- \leftrightarrow Fe(CN)_6^{4-}, \quad E^\circ = 0.36\ V \tag{1}$$

In the Supporting Information, Figure S2, the cyclic voltammograms of Pt/WO_3, Pt/WC, and Pt/C in N_2 saturated 0.01 M $K_3Fe(CN)_6$, 0.01 M $K_4Fe(CN)_6$, 0.1 M $HClO_4$ solution between 0 and 0.9 V are compared. In all cases, $Fe(CN)_6^{3-}$ was electrochemically generated from $Fe(CN)_6^{4-}$ in the forward scan, demonstrated by an anodic peak, and then was reduced back to $Fe(CN)_6^{4-}$ in the reverse scan with a cathodic peak. For a perfectly reversible process, the number of electrons are related to the difference of peak potentials by

$$E_{pa} - E_{pc} = \frac{59\ mV}{n} \tag{2}$$

Here, E_{pa} and E_{pc} are the anodic and cathodic peak potential, separately. The distances of the anodic and cathodic current peaks of Pt/C (0.20 V) and Pt (0.15 V) were bigger than those of the Pt/WC (0.09 V) and Pt/WO_3 (0.10 V), which implied that the electron transfer process was more efficient on Pt/WC and Pt/WO_3 than Pt/C. The high surface area of the platinum nanoparticles supported on the microporous structure WC and nanosize WO_3 crystals could facilitate the efficient mobility for electrons, improving performance compared with bulk Pt perhaps by modifying the electronic structure of the supported Pt nanoparticles.

3.5. Oxygen Reduction Activity of Pt Clusters Supported on WO_3. Cyclic voltammograms of Pt/WO_3 in O_2 saturated 0.1 M $HClO_4$ at 10 mV/s and 50 mV/s are shown in Supporting Information, Figure S3. Typically well-defined hydrogen adsorption/desorption peaks, corresponding to the various Pt crystallographic planes, were observed. By integrating the current density in the hydrogen adsorption/desorption region after double-layer correction, the specific electrochemically active surface area (ECSA) (per unit weight of Pt) was calculated by the following equation:[23]

$$S_e = \frac{Q_r}{m \times C} \tag{3}$$

Where m is the mass loading of Pt on the working electrode, Q_r is the H_2 under potential desorption charge, C is the charge needed to oxidize one layer of hydrogen on Pt (0.21 mC cm^{-2} for polycrystalline Pt[24]). The ECSA calculated based on the 50 mV/s curve was 63.2 m^2/g_{Pt}, similar to that of Pt/C at the same scan rate reported previously.[25,26] Considering the much smaller surface area of the nanosize WO_3 substrate compared with the carbon supports (~15%), improved Pt utilization due to the homogeneous dispersion of Pt nanoparticles likely contributed to an identical ESCA value.

Positive going linear sweep voltammograms are presented in Figure 3 for a Pt/C electrode, Pt supported on commercial WO_3 (Pt/WO_3), and nanosize Pt/WO_3 prepared in this study (nano-Pt/WO_3). The ORR onset and half-wave potentials of

dx.doi.org/10.1021/cs200657w | ACS Catal. 2012, 2, 456−463

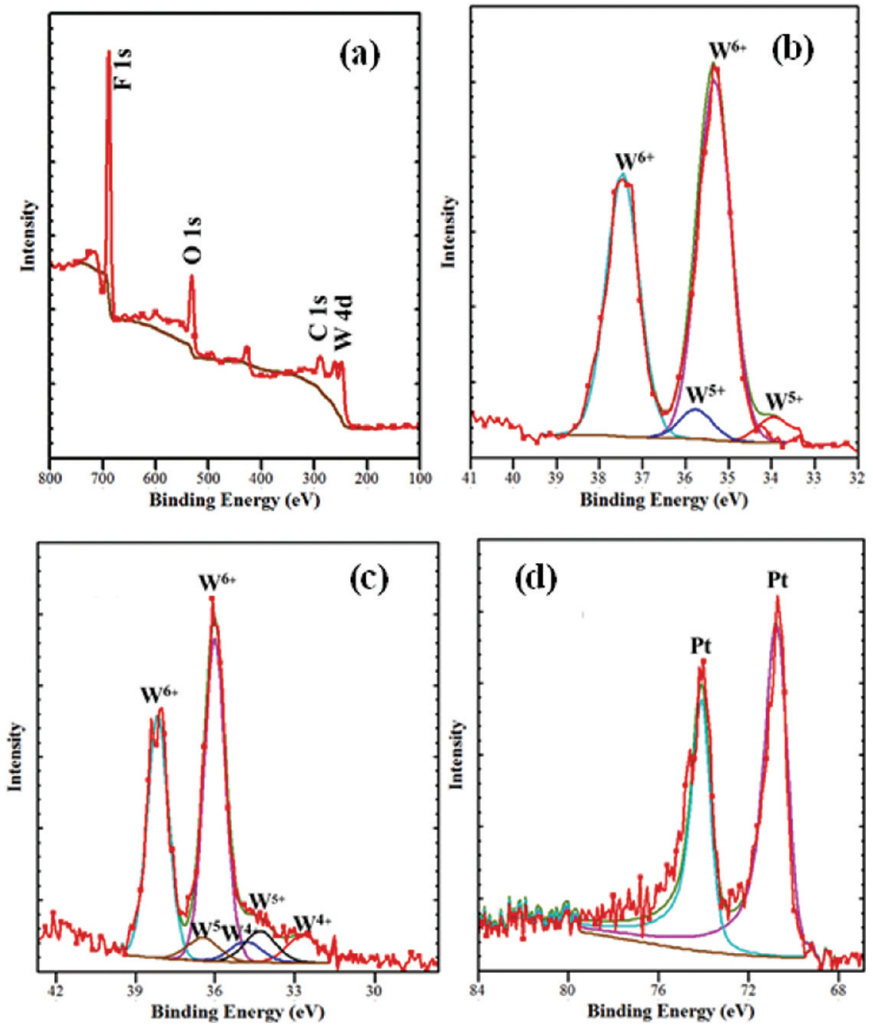

Figure 2. XPS spectra of WO_3 crystal and Pt/WO_3 catalyst: (a) general region and (b) W(4f) regions (for the WO_3 crystal) and (c) W(4f) and (d) Pt(4f) regions (for the Pt/WO_3 catalyst).

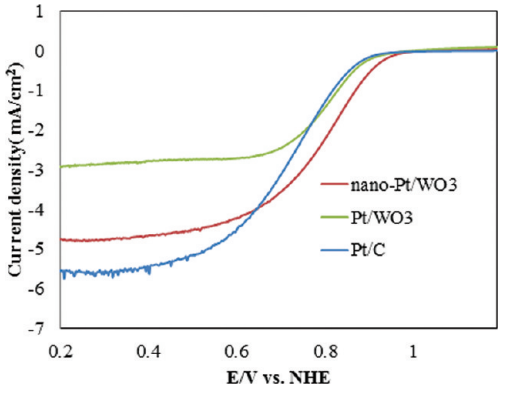

Figure 3. Linear sweep voltammograms for thin film Pt/C, commercial Pt/WO_3, and nano-Pt/WO_3 electrocatalysts in O_2-saturated 0.1 M $HClO_4$; 10 mv/s, 1600 rpm.

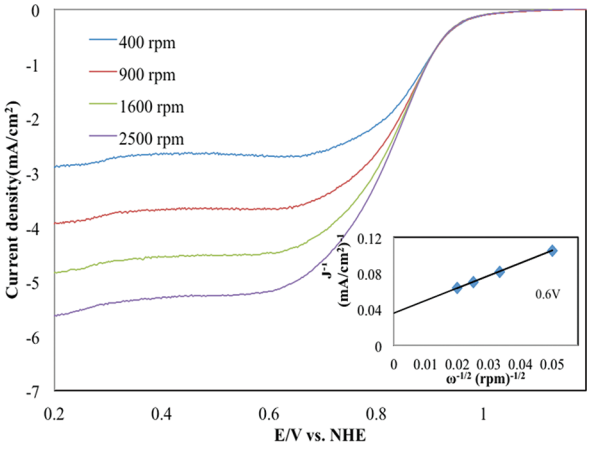

Figure 4. Linear sweep voltammograms for thin film Pt/WO_3 electrocatalysts in O_2-saturated 0.1 M $HClO_4$; 5 mV/s, 400 rpm, 900 rpm, 1600 rpm, 2500 rpm. Inset. J^{-1} Versus $\omega^{-1/2}$ plot for the ORR on Pt/WO_3 at 0.6 V.

the commercial Pt/WO_3 were comparable with Pt/C. However, the nano-Pt/WO_3 showed a significant improvement in ORR activity relative to Pt/C, which was evidenced by a large shift in both the ORR onset and the half-wave potentials. Combined with the XPS data, it appears that the stronger metal interaction between nanosized WO_3 support and Pt nanoparticles indeed modified the Pt electronic structure, facilitating improved activity.

To address this more clearly, positive going linear sweep voltammograms for oxygen reduction at Pt/WO_3 catalyst in 0.1 M $HClO_4$ are shown as a function of disk rotation rate from 400 rpm to 2500 rpm in Figure 4. Inset within Figure 4 is a

dx.doi.org/10.1021/cs200657w | ACS Catal. 2012, 2, 456–463

typical Koutecky–Levich plot, which (assuming first order kinetics) allows researchers to separate effects of kinetics and mass transfer by plotting the inverse of the current density (J^{-1}) versus the inverse of the square root of the rotation rate ($\omega^{-1/2}$):[27]

$$\frac{1}{J} = \frac{1}{J_k} + \frac{1}{J_{diff}} = \frac{1}{J_k} + \frac{1}{B\omega^{1/2}} \quad (4)$$

where J_k is the kinetic current density and J_{diff} the diffusion-limited current density. At each potential, the intercept of the Koutecky–Levich plot is J_k^{-1} and the slope is equal to $1/B$, where B is given by eq 5.

$$B = 0.62nFC_0D_0^{2/3}\eta^{-1/6} \quad (5)$$

where F is the Faraday constant, n is the overall number of electrons transferred in the ORR, C_0 is the O_2-saturated concentration in the 0.1 M $HClO_4$ electrolyte (1.26×10^{-3} mol L^{-1}), D_0 is the diffusion coefficient of O_2 in the $HClO_4$ electrolyte (1.93×10^{-5} cm^2 s), and η is the viscosity of the electrolyte (1.009×10^{-2} cm^2 s).[28] In the J^{-1} versus $\omega^{-1/2}$ plot, the slope is $1/B$, as shown in the above equation, which can be applied to obtain the number of electrons involved in the ORR. The calculated theoretical value of B was 0.466 $(mA/cm^2)S^{-1/2}$. The number of electrons calculated from the slope of the Koutecky–Levich plots in this study was 3.7. This n value indicated that there was a nearly complete reduction of O_2 to H_2O, a four-electron process, on the surface of the Pt/WO_3 electrocatalyst.

Figure 5 shows the Tafel plot for the ORR on WO_3 at 1600 rpm observed in our work with the factor $I_k = \text{Log } I/(I_m - I)$

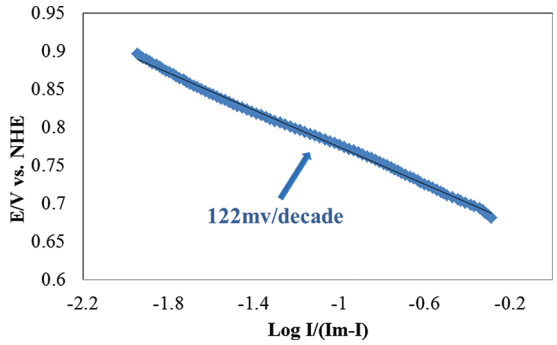

Figure 5. Tafel slope for oxygen reduction on the glassy carbon disk covered by a layer of Pt/WO_3 in 0.1 M $HClO_4$. Rotation rate: 1600 rpm.

used to obtain the current under kinetic control. Surprisingly, a single Tafel slope was observed over the entire potential window, and was found to be 122.2 mV/dec. This was the first direct evidence of SMSI between Pt and WO_3 since the Tafel slope of Pt catalysts is dictated by its surface oxidation state as a function of potential.[29] Typically, Pt in $HClO_4$ electrolyte shows two slopes. There is a "low" 60 mV/dec Tafel slope at high potentials, followed by a 120 mV/dec slope at lower potentials. These two slopes are attributed to the formation and adsorption of surface oxides on the Pt surface, mainly PtOH and PtO, which are derived from the reaction of H_2O with Pt.[29]

$$Pt + H_2O \rightarrow Pt - OH_{ads} + H^+ + e^-$$
$$E^0 = 0.85 - 1.10\ V \quad (6)$$

$$Pt + H_2O \rightarrow PtO + 2H^+ + 2e^- \quad (7)$$

These oxides inhibit the ORR, and influence the performance of PEM fuel cells directly. Here the constant high Tafel slope of Pt/WO_3 implies that with the WO_3 as the support material, Pt–OH formation is pushed to higher potentials, leaving a clean, highly active Pt surface for the ORR. In addition, the PtO can further dissolve in the PEM fuel cell cathode through the following reaction:

$$PtO + 2H^+ \rightarrow Pt^{2+} + H_2O \quad (8)$$

which can lead to the dissolution of smaller Pt clusters, and resulting Pt^{2+} ions that are subsequently redeposited on larger Pt clusters, plated somewhere else within the cathode or even in the PEM, which leads to the degradation of fuel cell performance. Pt/WO_3 may also help in preventing this catalyst degradation mechanism.

3.6. Electrochemical Stability of Raw and Platinized WO_3 Supports. For supported electrocatalysts, surface stability becomes especially crucial to device operation as the loss of the top supported layer will result in a complete change in the electrocatalytic activity. To test the stability of the monolayer Pt/WO_3 samples studied here, platinized WO_3 was electrochemically cycled between 0.0 and 1.4 V 300 times at 10 mV/s. The results are presented in Figure 6. It is obvious

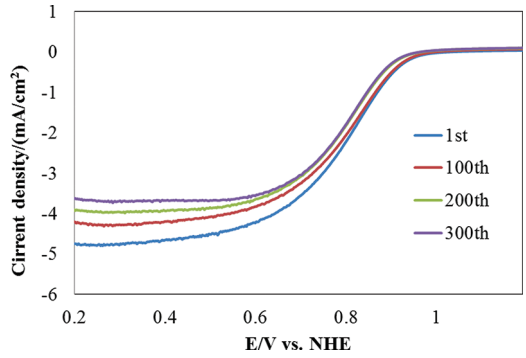

Figure 6. Linear sweep voltammograms for Pt/WO_3 electrocatalysts on their 300 cycles in O_2 saturated 0.1 M $HClO_4$ at 1600 rpm; scan rate: 10 mV/s.

that the onset and half-wave potentials of the Pt/WO_3 for the ORR shifted negative, which suggests that the activity of the Pt/WO_3 was reduced during the stability test and the Pt/WO_3 electrocatalysts were unable to keep their superior performance during cycling. To probe the performance degradation mechanism of Pt/WO_3, first, the stability of raw WO_3 support was investigated.

Cyclic voltammograms were obtained for raw WO_3 on glassy carbon electrodes in O_2-saturated 0.1 M $HClO_4$ at room temperature to investigate their redox stability in the potential window relevant to the ORR, shown in Figure 7. The potential was cycled between 0.0 and 0.3 V first, then the positive end of the potential window was extended by 100 mV in each subsequent experiment. This was repeated until the threshold potential was 1.4 V. Figure 7 shows the results for the potential window opening experiments on the thin film WO_3 electrode. In the oxygenated electrolyte, WO_3 showed some activity for hydrogen adsorption/desorption between 0.0 and 0.35 V and, different from our previous work on WC supports, there were no obvious corrosion oxidation or reduction peaks observed in the ORR regime at elevated potentials.

dx.doi.org/10.1021/cs200657w | ACS Catal. 2012, 2, 456–463

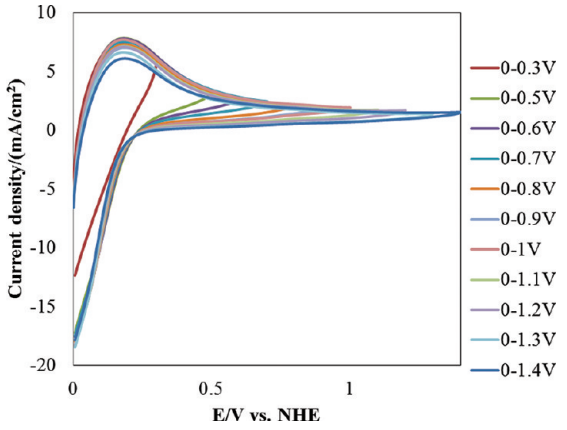

Figure 7. Cyclic voltammograms of raw WO_3 in O_2 saturated 0.1 M $HClO_4$, scanrate is 50 mV/s.

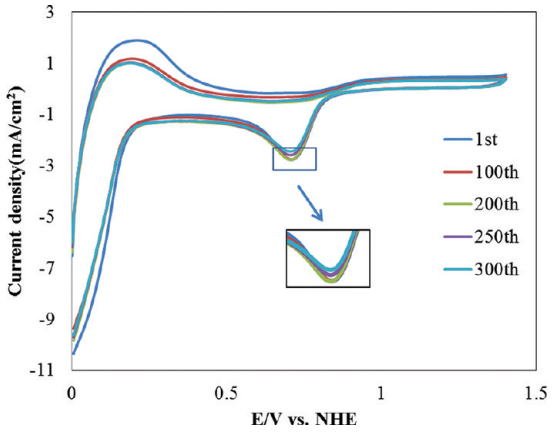

Figure 8. Cyclic voltammograms of Pt/WO_3 in O_2 saturated 0.1 M $HClO_4$ between 0 and 1.4 V for 300 cycles; scan rate is 10 mV/s.

However, integrating the hydrogen adsorption charge between 0.0 and 0.35 V showed a slight increase as a function of threshold potential. There are two possible reasons to explain the increase: First, a competing reduction reaction occurs in this potential range. Second, more hydrogen was adsorbed on the WO_3 surface by spillover from Pt. Also, it has been reported that tungsten oxide can form stable hydrogen tungsten bronze, H_xWO_3, and substoichiometric oxides, WO_{3-y}, by reaction with hydrogen:[30]

$$WO_3 + xH^+ + xe^- \rightarrow H_xWO_3 \qquad (0 < x < 1) \tag{9}$$

$$WO_3 + 2yH^+ + 2ye^- \rightarrow WO_{3-y} + yH_2O \tag{10}$$

It is well-known that tungsten oxide (WO_3) is an electrochromic (color change by applying electric field) material[31,32] and shows a wide range of colors depending on its reductive state. This is shown in Supporting Information, Figure S4, where the color of Na_xWO_3 changes correspondingly with the different degrees of W^{6+} reduction.[33] On the basis of our observation, the color of tungsten oxide turned from yellow-green to dark blue, which indicated that tungsten bronze was present on the catalyst support surface. Kulesza and Faulkner reported there are characteristic reduction peaks at 0.22 and 0.08 V (vs NHE) in cyclic voltammetry graph of Pt/WO_3 on graphite[34] that overlap with two of the hydrogen adsorption/desorption peaks on polycrystalline Pt. This suggests that the expanding of the hydrogen adsorption peaks can be seen as both a sign of WO_3 reduction to form hydrogen tungsten bronze, and an enhanced adsorption of hydrogen to form the hydrogen tungsten bronze, eq 11.

$$PtH_{ads} + WO_3 = Pt + H_xWO_3 \tag{11}$$

However, tungsten bronzes are mildly soluble in acid media and can dissolve slowly. This effect has the potential to undermine the stability of Pt/WO_3 catalysts, leading to Pt detachment and a loss of SMSI effects, including high ORR activity of supported Pt.

CVs of platinized supports were also collected between 0.0 and 1.4 V in O_2-saturated electrolyte over 300 cycles. Scans 1, 100, 200, 250, 300 are shown in Figure 8. From these voltammograms, it is clear that there is a significant change between the first and 300th cycle, although for the first 200 cycles, the curves were similar. After 200 cycles, the magnitude and definition of the Pt surface oxide formation and reduction peaks diminished with increasing number of scans, which suggested that the Pt electrochemically active area and ORR activity were decreasing. The reason for the Pt active area decrease was explored by TEM. TEM images of the platinized supports after cycling 300 times between 0.0 and 1.4 V are shown in Figure 9. Compared with the Pt clusters shown in Figure 2, which were deposited homogeneously on the tungsten oxide surface with the average size of 3 nm, the Pt particles formed large agglomerates, ranging from 20 to 50 nm in size, which appeared to consist of detached 3 nm Pt particles. This is nearly identical to what we observed with Pt/WC catalysts.[18] The detachment and agglomeration of Pt particles were most probably due to the dissolution of surface tungsten bronze, which forced the Pt clusters from the surface, resulting in agglomerated Pt nanoparticle catalysts with no interaction with the WO_3 support, eliminating the SMSI activity enhancement.

Post cycling XPS spectra were collected to determine the difference in the surface composition before and after cycling 300 times on Pt/WO_3, and the graphs are shown in Figure 10. On the basis of the XPS data, two interesting features were observed. First, the atomic ratio of Pt to W, calculated from the areas of the Pt_{4f} and W_{4f} XPS peaks, decreased considerably, from 1.43 to 0.36. This was most likely because of the detachment and agglomeration of the surface Pt nanoparticles; the formed Pt superclusters would significantly decrease the observed atomic Pt/W ratio. Also, after stability tests, only 29.84% of the surface W was identified as WO_3, with the remaining present as W^{5+}(from both synthesized W_2O_5 and formed hydrogen tungsten bronze) and W^{4+}.

3.7. Mechanism for Activity Loss of Pt/WC and Pt/WO_3 as ORR Electroatalysts. In our previous paper,[18] although the Pt/WC was found to have a high activity toward the ORR, the WC surface was oxidized to WO_x at potentials relevant to the ORR (>0.8 V); this oxidation was followed by surface roughening and deformation as well as the detachment and agglomeration of Pt clusters on WC crystals, which eliminated the synergistic effect observed on as-prepared Pt/WC. In this study, by directly using nanosize WO_3 as the supports for Pt nanoparticles, the activity and stability of Pt/WO_3 was investigated. The Pt/WO_3 electrocatalyst showed good activity for ORR (Figure 4, 5), and superior electron transfer ability compared to conventional Pt/C and bulk polycrystalline Pt (Supporting Information, Figure S2).

dx.doi.org/10.1021/cs200657w | ACS Catal. 2012, 2, 456–463

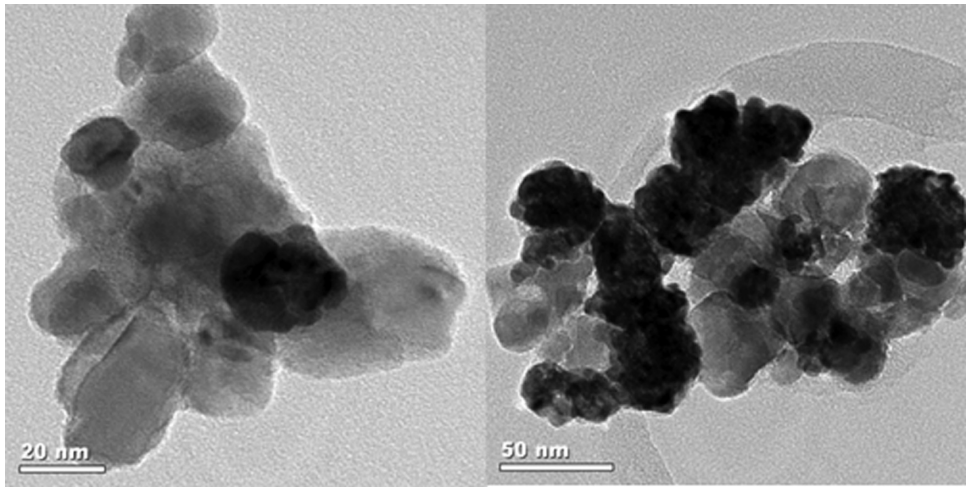

Figure 9. TEM image of Pt/WO_3 after cycling between 0 and 1.4 V 300 times.

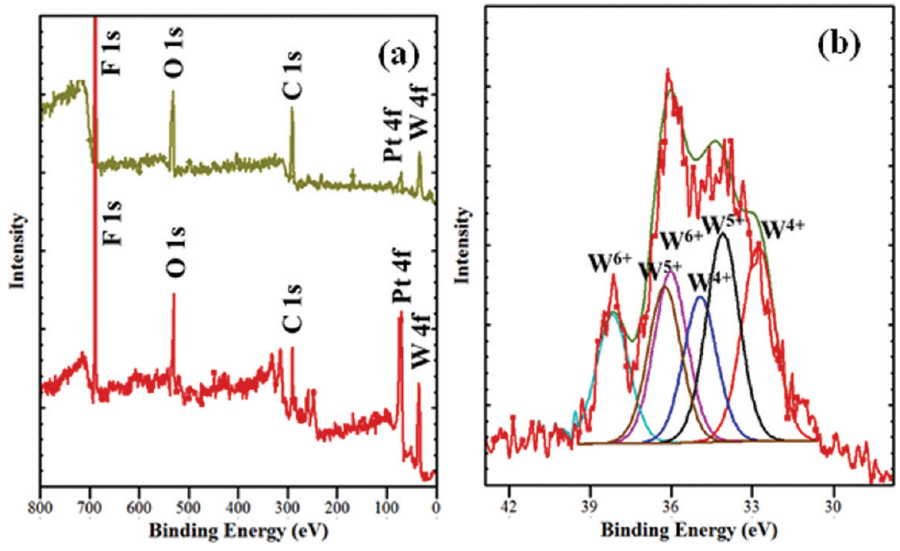

Figure 10. XPS image of Pt/WO_3 before (a) and after (b) cycling between 0 and 1.4 V 300 times.

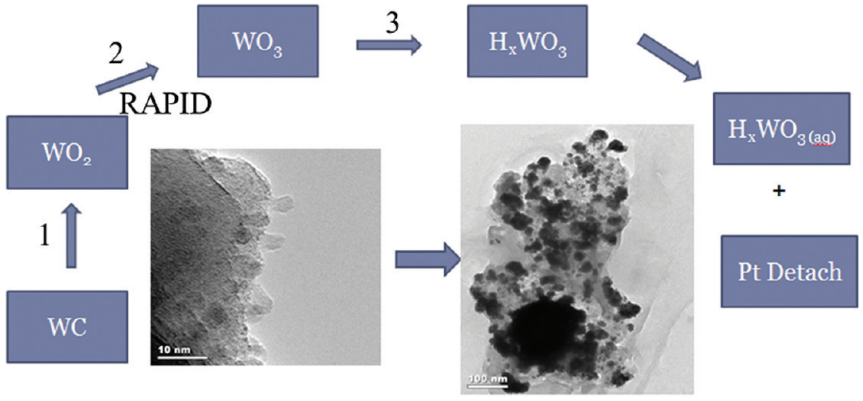

$$\bullet WC(s) + 4H_2O \rightarrow WO_2(s) + CO_2(g) + 8H^+ + 8e^-$$
$$\bullet WO_2(s) + H_2O(l) \rightarrow WO_3(s) + 2H^+ + 2e^-$$
$$\bullet WO_3 + xH^+ + xe^- \rightarrow H_xWO_3$$

Figure 11. Mechanism for ORR Activity Loss and Pt Agglomeration on Pt/WC and Pt/WO_3 Electrocatalysts.

However, from this study, it was clear that WO_3 easily formed water-soluble hydrogen tungsten bronze (H_xWO_3) in the hydrogen adsorption region. Furthermore, the monolayer Pt deposited on tungsten oxide crystals could also accelerate

dx.doi.org/10.1021/cs200657w | ACS Catal. 2012, 2, 456–463

H_xWO_3 formation since Pt itself has high hydrogen adsorption ability. In both cases, the hydrogen tungsten bronze species dissolved into the acid electrolyte and caused the detachment of Pt nanoparticles from the oxidized tungsten surface.

In summary, WC and WO_3 as Pt supports during the ORR is shown in Figure 11. On WC, performance degradation is initiated by electrochemical oxidation of WC to WO_x at E > 0.8 V. Next, the surface is further oxidized to WO_3 and is so energetically favored that it occurs fairly rapidly over the entire potential window. These WO_3 sites are slightly reduced during the ORR to hydrogen tungsten bronze species, which are soluble in acid media; this solubility facilitates the detachment of Pt particles from the surface. Detached Pt particles not only lose the high synergistic activity, they also agglomerate, severely reducing the Pt mass activity over time. On WO_3 supports, the potential dependence of the degradation behavior is removed and reduction to H_xWO_3 and subsequent dissolution and detachment of Pt slowly occurs during testing.

4. CONCLUSION

WO_3 was investigated as an electrocatalyst support material for monolayer Pt, and the Pt/WO_3 was evaluated as an electrocatalyst for the ORR. It was found that Pt/WO_3 showed a good activity for ORR and superior electron transfer ability compared to conventional Pt/C and Pt. However, WO_3 easily formed water-soluble hydrogen tungsten bronze (H_xWO_3), which facilitated the detachment of Pt nanoparticles. This result also pointed to a new degradation mechanism for WC instability in acid media, which included the sequential electrochemical oxidation of WC to WO_x and WO_3 at E > 0.8 V, followed by the formation and dissolution of H_xWO_3. The proposed degradation mechanism for WC and WO_3 suggests that as long as the support surface is exposed to the acidic electrolyte, neither represents a long-term stable support material for Pt electrocatalysts. This does; however, raise interesting questions about alternative structures (i.e., Pt-WC or Pt-WO_3 core shell structures) for novel high activity ORR catalysts.

■ ASSOCIATED CONTENT

Supporting Information

Further details are given about powder XRD patterns for pure tungsten oxide crystals, cyclic voltammograms of Pt/WO_3, Pt/WC, and Pt/C in $K_3Fe(CN)_6$ and $K_4Fe(CN)_6$ solution and of Pt/WO_3 in $HClO_4$ acid, and the color of Na_xWO_3 with different x values. This material is available free of charge via the Internet at http://pubs.acs.org.

■ AUTHOR INFORMATION

Corresponding Author

*Phone: 860-486-2756. Fax: 860-486-2959. E-mail: mustain@engr.uconn.edu.

Notes

The authors declare no competing financial interest.

■ REFERENCES

(1) Gasteiger, H. A.; Mathias, M. F. In *Proton Conducting Membrane Fuel Cells II*; Murthy, M., Fuller, T. F., Van Zee, J. W., Gottefeldt, S., Eds.; The Electrochemical Society Proceedings Series: Pennington, NJ, 2005; PV 2002-31, p 1.
(2) Shao, Y.; Liu, J.; Wang, Y.; Lin, Y. *J. Mater. Chem.* **2009**, *19*, 46.
(3) Shrestha, S.; Liu, Y.; Mustain, W. E. *Catal. Rev.* **2011**, *53*, 256.
(4) Suntivich, J.; May, K. J.; Gasteiger, H. A.; Goodenough, J. B.; Shao-Horn, Y. *Science* **2011**, *334*, 1383.
(5) Roen, L. M.; Paik, C. H.; Jarvi, T. D. *Electrochem. Solid-State Lett.* **2004**, *7*, A19.
(6) Tauster, S. J.; Fung, S. C.; Garten, R. L. *J. Am. Chem. Soc.* **1978**, *100*, 170.
(7) Fu, Q.; Wagner, T. *Surf. Sci. Rep.* **2007**, *62*, 431.
(8) Lemonidou, A. A.; Nalbandian, L.; Vasalos, I. A. *Catal. Today.* **2000**, *61*, 333.
(9) Hammer, B.; Nørskov, J. K. *Adv. Catal.* **2000**, *45*, 71.
(10) Lee, S. H.; Deshpande, R.; Parilla, P. A.; Jones, K. M.; To, B.; Mahan, A. H.; Dillon, A. C. *Adv. Mater.* **2006**, *18*, 763.
(11) Supothina, S.; Seeharaj, P.; Yoriya, S.; Sriyudthsak, M. *Ceram. Int.* **2007**, *33*, 931.
(12) Shukla, A. K.; Ravikumar, M. K.; Roy, A.; Barman, S. R.; Sarma, D. D. *J. Electrochem. Soc.* **1994**, *114*, 1517.
(13) Shukla, A. K.; Ravikumar, M. K.; Aricò, S.; Candiano, G.; Antonucci, V.; Giordano, N.; Hamnett, A. *J. Appl. Electrochem.* **1995**, *25*, 528.
(14) Ganesan, R.; Lee, J. S. *J. Power Sources.* **2006**, *157*, 217.
(15) Nagel, T.; Bogolowski, N.; Samjeske, G.; Baltruschat, H. *J. Solid State Electrochem.* **2003**, *7*, 614.
(16) Roth, C.; Goetz, M.; Fuess, H. *J. Appl. Electrochem.* **2001**, *31*, 793.
(17) Chen, K. Y.; Sun, Z.; Tseung, A. C. C. *Electrochem. Solid-State Lett.* **2000**, *3*, 10.
(18) Liu, Y.; Mustain, W. E. *ACS Catalysis.* **2011**, *1*, 212.
(19) Esposito, D. V.; Chen, J. G. *Energy Environ. Sci.* **2011**, *4*, 3900.
(20) Esposito, D. V.; Hunt, S. T.; Stottlemyer, A. L.; Dobson, K. D.; McCandless, B. E.; Birkmire, R. W.; Chen, J. G. *Angew. Chem., Int. Ed.* **2010**, *49*, 9859.
(21) Hu, W. B.; Zhu, Y. Q.; Hsu, W. K.; Chang, B. H.; Terrones, M.; Grobert, N.; Terrones, H.; Hare, J. P.; Kroto, H. W.; Walton, D. R. M. *Appl. Phys. A: Mater. Sci. Process.* **2000**, *70*, 231.
(22) Beard, B. C.; Ross, J. P. N *J. Electrochem. Soc.* **1986**, *133*, 1839.
(23) Ryan, S. H.; et al. *Nanotechnology* **2010**, *21*, 165705.
(24) Pozio, A.; De Francesco, M.; Cemmi, A.; Cardellini, F.; Giorgi, L. *J. Power Sources.* **2002**, *105*, 13.
(25) Lim, B.; Jiang, M.; Camargo, P. H. C.; Cho, E. C.; Tao, J.; Lu, X.; Zhu, Y.; Xia, Y. *Science* **2009**, *324*, 1302.
(26) Zhang, H.; Lin, R.; Cao, C.; Zhao, J.; Ma, J. *Electrochim. Acta* **2011**, *56*, 7622.
(27) Anastasijević, N. A.; Vesović, V.; Adžić, R. R. *J. Electroanal. Chem. Interfaces* **1987**, *229*, 305.
(28) Marković, N. M.; Gasteiger, H. A.; Grgur, B. N.; Ross, P. N. *J. Electroanal. Chem.* **1999**, *467*, 157.
(29) Wang, J. X.; Markovic, N. M.; Adzic, R. R. *J. Phys. Chem. B.* **2004**, *108*, 4127.
(30) Shim, J.; Lee, C.-R.; Lee, H.-K.; Lee, J.-S.; Cairns, E. J. *J. Power Sources.* **2001**, *102*, 172.
(31) Bechinger, C.; Burdis, M. S.; Zhang, J. G. *Solid State Commun.* **1997**, *101*, 753.
(32) Kim, J. J.; Tryk, D. A.; Amemiya, T.; Hashimoto, K.; Fujishima, A. *J. Electroanal. Chem.* **1997**, *435*, 31.
(33) Ellis, A. B.; Geselbracht, M. J.; Johnson, B. J.; Lisensky, G. C.; Robinson, W. R. *Teaching General Chemstry: A Materials Science Companion*; American Chemical Society: Washington, DC, 1993; p 415.
(34) Kulesza, P. J.; Faulkner, L. R. *Colloids Surf.* **1989**, *41*, 123.